Optical Engineering

OpticalEngineering.SPIEDigitalLibrary.org

Design of three-dimensional structured-light sensory systems for microscale measurements

Veronica E. Marin
Zendai Kashino
Wei Hao Wayne Chang
Pieter Luitjens
Goldie Nejat

Veronica E. Marin, Zendai Kashino, Wei Hao Wayne Chang, Pieter Luitjens, Goldie Nejat, "Design of three-dimensional structured-light sensory systems for microscale measurements," *Opt. Eng.* **56**(12), 124109 (2017), doi: 10.1117/1.OE.56.12.124109.

Optical Engineering 56(12), 124109 (December 2017)

Design of three-dimensional structured-light sensory systems for microscale measurements

Veronica E. Marin, Zendai Kashino,* Wei Hao Wayne Chang, Pieter Luitjens, and Goldie Nejat
University of Toronto, Autonomous Systems and Biomechatronics Laboratory, Department of Mechanical and Industrial Engineering, Toronto, Canada

Abstract. Recent advances in precision manufacturing have generated an increasing demand for accurate microscale three-dimensional metrology approaches. Structured light (SL) sensory systems can be used to successfully measure objects in the microscale. However, there are two main challenges in designing SL systems to measure complex microscale objects: (1) the limited measurement volume defined by the system triangulation and microscope optics and (2) the increased random noise in the measurements introduced by the microscope magnification of the noise from the fringe patterns. In a paper, a methodology is proposed for the design of SL systems using image focus fusion for microscale applications, maximizing the measurement volume and minimizing measurement noise for a given set of hardware components. An empirical calibration procedure that relies on a global model for the entire measurement volume to reduce measurement errors is also proposed. Experiments conducted with a variety of microscale objects validate the effectiveness of the proposed design methodology. [DOI: 10.1117/1.OE.56.12.124109]

Keywords: metrology; three dimensions; fringe analysis.

Paper 171285 received Aug. 15, 2017; accepted for publication Nov. 28, 2017; published online Dec. 28, 2017.

1 Introduction

Recent advances in precision manufacturing[1,2] have generated an increasing demand for the development of efficient and accurate microscale three-dimensional (3-D) metrology approaches. Microscale manufacturing has enabled many revolutionary devices in varying applications such as implanted microrobots and wireless swallowable capsules in biomedicine,[3,4] microlens arrays in optics,[5] and nanodrones in aerospace,[6] with feature sizes in the range of 1 μm to 10 mm. These applications pose significant challenges to current 3-D metrology techniques, such as coordinate measurement machines, laser interferometry, and stereomicroscopy, in terms of measurement speed, accuracy, robustness, and ability to handle surfaces of arbitrary complexity.[2]

A number of challenges need to be addressed when measuring complex microscale objects. For example, traditional optical approaches cannot be directly used to measure complex objects in the microscale domain due to their limited depth of field (DOF), the short focal lengths of optical microscopes, and the reduction of the signal-to-noise ratio when objects are magnified.[2] In particular, it is not possible to keep the entire object in focus; therefore, only a portion of the object can be measured with a single point of view and focus setting. Thus, to overcome these problems, robust algorithms need to be developed to cope with noisy images due to the magnification used.[2]

In this work, we define complex objects as those that have large surface gradients and/or surface discontinuities such as sharp edges, holes, and grooves, while simple objects refer to those that have smooth surface profiles with gradients similar to plane surfaces. To date, structured light (SL) sensory systems with digital fringe projection technology,[7–14] laser interferometry,[15,16] and digital holographic microscopy[17,18] have been successfully developed to measure objects at the microscale. Of the three, SL sensory systems have emerged as a popular method for measurement due to their ability to (1) measure surfaces without scanning,[19] (2) provide accurate and real-time measurements,[7] and (3) make use of off-the-shelf hardware components for implementation.[20]

SL systems have been developed following two approaches: (1) modifying stereomicroscopes to include fringe pattern projection[8–10] or (2) integrating microscope lenses with a camera and a projector and placing them in an arbitrary triangulation configuration.[7,11–14] These SL systems were able to show the potential of using SL technology to measure different microscale objects. However, this was done within a limited measurement volume, which was imposed by the triangulation configuration and the microscope optics specifications. Furthermore, the fringe patterns used by these SL systems need to explicitly consider the effect of low signal-to-noise ratio that arises from microscope magnification when obtaining microscale 3-D measurements. Hence, a detailed investigation needs to be conducted to define the design constraints for developing SL systems to measure microscale objects to obtain the most accurate measurements given a set of hardware components.

Our previous research in this area comprises the development of design methodologies: to determine the hardware triangulation configuration of SL systems without microscope lenses[21] and the optimal patterns for reducing random noise in 3-D measurements for these SL systems.[22] In this paper, we present a comprehensive design methodology and calibration procedure needed for the development and calibration of SL sensory systems with microscope lenses,

*Address all correspondence to: Zendai Kashino, E-mail: zendkash@mie.utoronto.ca

0091-3286/2017/$25.00 © 2017 SPIE

using image focus fusion to effectively increase the measurement volume. In contrast with iterative, *ad hoc* design approaches for SL systems, the proposed design methodology extends our previous work[21,22] to uniquely provide a formal procedure to determine the optimal design of the hardware triangulation configuration and the corresponding fringe patterns to obtain SL systems for accurate microscale measurements. The proposed calibration procedure takes into account image focus fusion and fits a single, empirical, global calibration model, which is valid across all camera and projector pixel coordinates, to all calibration data for narrower confidence intervals on predictions.

Our unique methodology first considers the specifications of the microscope lenses to determine the triangulation configuration that provides the maximum measurement volume. Then, it minimizes the increased noise that is a direct result of microscope magnification by identifying the optimal fringe patterns that will minimize the random noise in the 3-D measurements. After these two stages have been implemented, a calibration procedure is utilized to provide the necessary global calibration model for the increased measurement volume. The proposed design methodology and the calibration procedure are implemented on an SL system, and its performance is validated by measuring objects with varying surface profiles.

2 3D SL Systems for Microscale Measurements

This section provides an overview of the related work on the SL systems proposed for microscale measurements. First, existing SL systems developed for microscale measurements are presented. Then, calibration procedures for such systems are discussed.

2.1 *Development of Microscale Systems*

Numerous structured-light systems have been developed for microscale measurements. As in macroscale SL systems, these systems make use of both imaging and pattern projection hardware. Imaging hardware usually consists of charge-coupled device (CCD)[8,10–12] or complementary metal-oxide-semiconductor (CMOS)[14] cameras. Pattern projection, on the other hand, includes a variety of methods to project SL patterns onto the object of interest. These include sinusoidal grating with an light-emitting diode light source,[8] a matrix-shaped array of pinholes to create light dots,[9] and fringe projection using liquid-crystal display[11,12] and digital micromirror device (DMD)[10,14] projectors. Furthermore, all microscale SL systems also make use of some micro-imaging optics such as long working distance microscope lenses[11,12,14] and stereomicroscopes[8] to both view and project the patterns onto objects of interest.

While most systems are designed with static measurements in mind, some systems have been developed to achieve real-time performance. For example, in Ref. 10, a graphics processing unit was used to allow for parallel image acquisition and post-processing to render real-time images at a frame rate of ∼30 Hz. Other SL systems have been designed with special considerations such as increasing the DOF[14] and minimizing system size.[7] For example, in Ref. 14, the Scheimpflug principle was used to obtain the SL hardware configuration needed to increase DOF. In Ref. 7, an SL system consisting of a microphase-shifting sinusoidal fringe projector and CCD camera with long working distance (LWD) microscope lenses mounted on a rigid fixture was designed to have a compact footprint and measure out-of-plane displacements with submicron resolution.

In general, SL system performance has been typically evaluated in terms of the measurement error of reference objects such as coins[8,12] and spheres.[9] Reported errors range between 1 and 17 μm.[10,14]

2.2 *Calibration of Microscale SL Systems*

System calibration is important to the development of high-accuracy SL systems. The accuracy of the 3-D reconstruction depends on the accuracy with which model parameters can be estimated based on calibration data.[14] Calibration approaches that have been proposed in the literature for SL systems can be classified into two categories: (1) model-based approaches that rely on parameterized physical models of the system (e.g., pinhole and orthographic projection models), with model parameters that are estimated based on calibration data[14,23–25] and (2) empirical approaches that utilize statistically derived models to map the actual measured information (e.g., image coordinates) to the desired measurement variable (world coordinates of the object surface).[1,8]

In general, model-based and empirical calibration approaches have been proposed for SL systems to measure macroscale objects.[26–29] Some of these approaches even consider cases in which the camera and/or projector are out-of-focus by estimating pinhole camera model parameters from out-of-focus images.[27–29] However, calibration of SL systems for measuring microscale objects poses the following additional challenges: (1) microscale measurements require special lenses whose optics typically deviate from pinhole models, thus requiring new calibration approaches[23] and (2) these lenses usually have shallow DOF, thus limiting the volume in which the target object can be in focus. In particular, the shallow DOF poses a challenge for calibration approaches that rely on multiple images of a calibration object at different poses inside the measurement volume, therefore, limiting the set of independent measurements that can be made of the calibration object. This introduces collinearity and ill-conditioning problems when only few similar orientations are considered in the model fitting algorithms to determine calibration parameters. To deal with these challenges, several calibration approaches have been proposed specifically for microscale measurements.

2.2.1 *Model-based calibration for microscale measurements*

Driven by the challenges imposed by the required optics to measure microscale objects, the model-based approaches used for macroscale measurements have been analyzed and customized to address the challenges of microscale measurements.[14,23–25,30] SL-based 3-D surface profiling in macroscale applications has extensively used calibration approaches that estimate the intrinsic parameters of the camera and projector, as well as the extrinsic parameters of the SL system triangulation configuration,[23,24] based on pinhole optical models. However, microscale SL systems require special lenses whose optics deviate from these pinhole models.[23] Hence, alternative procedures have been presented for the calibration of microscale SL systems, as described below.

In Ref. 30, a calibration method was proposed for an SL 3-D microscopic system consisting of a projector using an LWD microscope lens, modeled with pinhole optics, and a camera with a telecentric lens, modeled as an orthographic projection of the scene with a constant magnification. In the proposed calibration procedure, intrinsic and extrinsic parameters of the projector and camera are obtained from multiple calibration images. In Ref. 14, a model-based calibration approach consisting of a general imaging model that mapped each pixel in the camera CCD sensor or the projector DMD panel with a unique light ray was used. Pixel-to-pixel correspondences obtained from absolute phase values served to identify homologous pixel pairs (from the same light ray). The mapping of pixels to light rays was established for each pixel and stored in a look-up table (LUT).

Such model-based calibration approaches are based on physical modeling of the system optics and require multiple images of the calibration object with different poses within the measurement volume to define a calibration data set with a large number of linearly independent samples. This makes model-based approaches unsuitable for SL systems for microscale measurements in which the large optical magnifications that are used result in shallow DOFs. For these reasons, the literature in microscale measurements focuses on empirical calibration models.

2.2.2 *Empirical calibration models for microscale measurements*

Empirical calibration models rely on linear regression to create a mathematical model that maps the surface profile of an object $S(x, y)$ to the captured phase values at a given location (x, y) on the imaging sensor. These empirically based mathematical models are usually referred to as phase-to-height equations. As an advantage, empirical calibration approaches can be used regardless of the optics of the system and are thus suitable for systems with pinhole lenses, telecentric lenses, or combinations thereof. Therefore, empirical calibration approaches are suitable for SL systems for microscale applications.

To calibrate an SL system empirically, the direction of the z-coordinate (also known as depth or range) is defined, typically aligned with the bisector of the angle between the optical axes of the camera and projector[1] or with the optical axis of the camera.[8] In Ref. 1, a flat calibration object was placed on precision microstages and imaged in a sequence of positions as it was moved along the z-coordinate. Then, a relationship was established between the known position of the calibration plane measured with respect to the reference plane and the change in phase value for that pixel with respect to the phase value that the pixel had when the calibration plane was placed in a reference position. In Ref. 8, the phase-to-height relationship was used. Namely, an empirical calibration model was proposed as a linear regression of the reciprocal of height as a function of the reciprocal of phase, with a different set of regression coefficients for each pixel, stored in an LUT.

Though empirical calibration approaches using LUTs can be used regardless of the optics model of the system, their main disadvantage, aside from their memory storage requirements, is that each pixel-specific regression model is fitted to a small data set containing only information about the height of the surface that is observed at that camera pixel. For instance, if during the calibration procedure the calibration object is imaged at 10 different locations in the z-coordinate, the LUT approach would require fitting one regression model for each pixel based on (at most) 10 data points. Due to the small number of data samples used to fit the regression model, the resulting model coefficients are sensitive to noise in the calibration data and result in a larger predictive variance, i.e., wider confidence intervals for the model predictions. Hence, in this work, as opposed to using LUTs and one regression model for each image pixel, we propose using a single, global calibration model fitted to all the calibration data for all pixels using the absolute phase values. Such a calibration model is valid for all pixels in the image and is able to predict, with narrower confidence intervals, the world coordinates of the object surface.

3 Design of SL Systems for Microscale Measurements

We present herein a design methodology that considers the characteristics of 3-D measurements obtained from an SL system that incorporates microscope lenses. This methodology consists of (1) determining the SL system configuration of the hardware components and (2) identifying the pattern sequence for the optimal SL system configuration obtained. The first step determines the optimal triangulation configuration of the projector, camera and a reference plane such that the measurement volume is maximized. Then, the second step provides the sequence of the fringe patterns for the SL system configuration determined in the previous step.

3.1 *SL System Configuration*

The triangulation configuration between the camera, projector, and the measured object directly affects measurement accuracy. Namely, hardware implementation issues such as physical interference, working distances of the lenses, field-of-view (FOV), and DOF can impose a set of geometrical constraints that can significantly limit design choices for the system triangulation configuration, as we noted in Ref. 21 for macroscale measurements. Hence, the first step in the development of an SL system for microscale measurements is the design of the hardware triangulation configuration.

The design methodology presented in Ref. 21 is adapted to SL systems using microscope lenses. Namely, the hardware triangulation configuration for the SL system for microscale measurements is designed using the methodology shown in Fig. 1, which consists of the following steps: (1) design problem definition, (2) design constraints identification, and (3) optimization of SL configuration. In the first step, design variables and performance metrics are defined given hardware specifications (i.e., camera and projector resolution, pixel size, and lens focal lengths) and the user-defined parameters. In the second step, design constraints posed by practical limitation of the hardware components are formulated. Finally, the constrained optimization problem formulated in the first two steps is solved in the third step by evaluating through simulation the measurement volume of the SL system. The output of this step is an optimal SL system configuration.

For SL systems for microscale measurements, the optimization objective is to maximize the size of the measurement volume V_m:

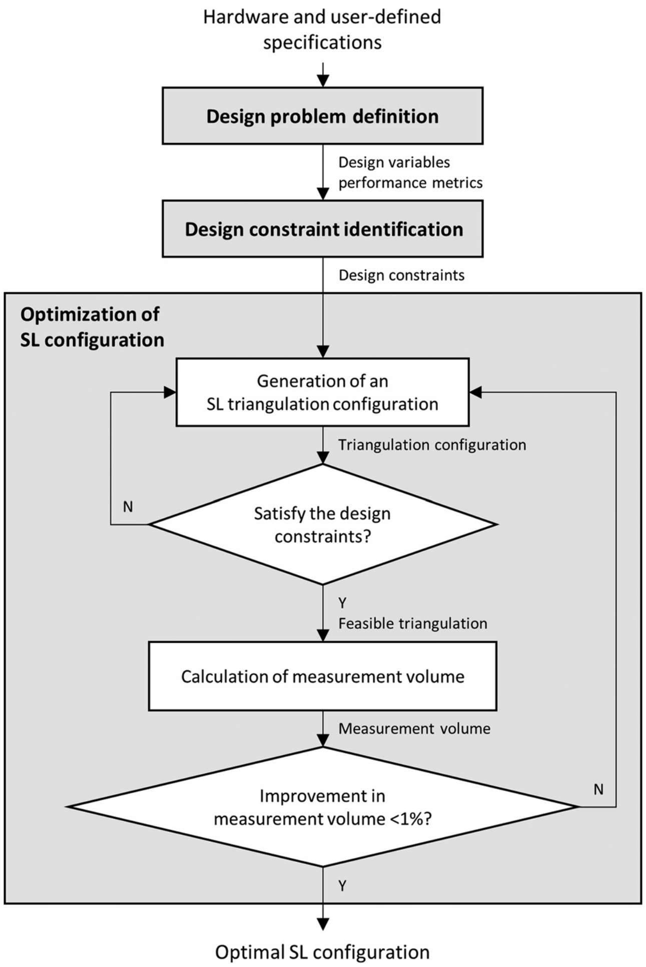

Fig. 1 Design procedure to determine the SL system configuration for microscale measurements.

$$\max V_m(\vec{u}), \quad \text{subject to } g(\vec{u}) \leq 0, \tag{1}$$

where $\vec{u} = (z_{\text{ref}}, w, l, h, \alpha_C, \beta_C)$ is the vector of (geometric) design variables and $g(\vec{u})$ is the vector of the constraints (e.g., no physical interference between the projector and camera hardware). The design variables consist of z_{ref}, which defines the position of a vertical reference plane where the camera and projector optical axes intersect; w (width), h (height), and l (length), which define the relative position of the camera with respect to the projector, and the angles (α_C, β_C), which correspond to the camera orientation.

Given the design objective and constraints above, an optimal system configuration will ensure that the SL system is using the maximum volume defined by the limited DOF and FOV imposed by the microscope lenses. Namely, this design methodology for the hardware configuration provides the optimal system triangulation that maximizes the overlap between the FOV and DOF of the camera and projector optics, while considering the design constraints defined to avoid physical interference of the hardware components. Optimization was carried out in an iterative manner until <1% improvement in the measurement volume was observed between iterations.

3.2 *SL Pattern Sequence for Optimal System Configuration*

Once the optimal system configuration has been determined, the design of the fringe patterns needs to consider the effect of random noise on the 3-D measurements. The 3-D coordinates are determined based on the projector-camera pixel-to-pixel correspondence, which is established by the absolute phase values obtained from a sequence of fringe patterns. To reduce the random noise in the absolute phase, a sequential phase unwrapping method is utilized, which first uses the absolute phase from a single-fringe pattern set to unwrap the relative phase from a multifringe pattern set and then progressively uses the resulting absolute phases from sets with increasing numbers of fringe patterns to unwrap the relative phase from the next set. The reduction in random noise in absolute phase values obtained by the sequential unwrapping of the pattern sequence is of particular importance during the calibration and the measurement steps at the microscale. As Sec. 5 will show, pixel-to-pixel correspondences, which are estimated from phase values, can introduce significant errors in the calibration data. Hence, the design methodology described in Ref. 22 is used for optimizing pattern sequences for SL microscale measurements. However, since the random noise in relative phase for SL systems with microscope lenses varies with the number of fringes, the random noise in relative phase of such SL systems is estimated based on all the number of fringes considered instead of using only the pattern with one fringe as in Ref. 22. The adapted design procedure for SL systems for microscale measurements, shown in Fig. 2, consists of the following tasks: (1) determining the feasible set of fringes for the SL system, (2) estimating the random noise in relative phase for each fringe pattern, and (3) identifying the set of fringe patterns that minimizes the random noise in the absolute phase resulting from sequential phase unwrapping.

The first task in the procedure is to determine the set of fringes $\mathbb{S}_n$ that will be considered for designing the pattern sequence, given the pattern resolution as an input. The pattern resolution is the number of pixels that will be used to encode the light patterns. For SL systems using sinusoidal phase-shifted light patterns that are encoded along one

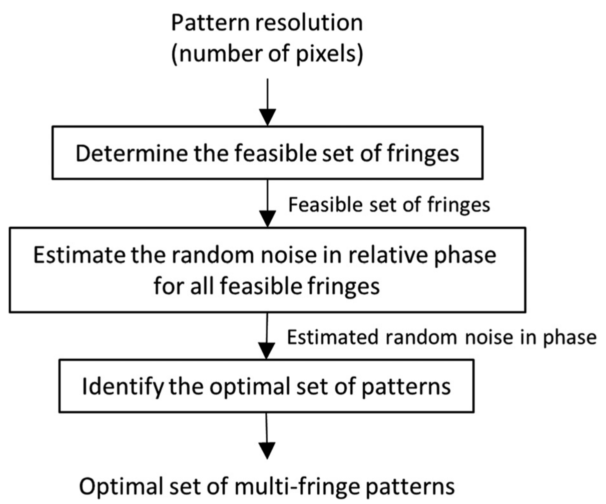

Fig. 2 Design procedure to determine SL pattern sequence for microscale measurements.

coding axis, the pattern resolution is the number of pixels of the DMD panel in the direction with the largest number of pixels, typically the horizontal direction n_H. Based on the pattern resolution, the largest number of fringes to be considered in $\mathbb{S}_n$ corresponds to the case in which the light pattern is encoded with at least 5 pixels per fringe, ensuring that the peaks and troughs of the sinusoidal wave are properly captured. In addition, to avoid aliasing during sequential phase unwrapping, the fringe patterns must encode all the pixels in the coding axis, i.e., the number of fringes must be an exact divisor of n_H. With these considerations, the set of fringes $\mathbb{S}_n$ is defined as $\mathbb{S}_n = \{n_f\}$, where $n_f \in \{1,2,\ldots,n_H/5\}$ and $n_H \bmod n_f = 0$.

The second task is to estimate the noise in the relative phase values caused by random noise in image intensity from the fringe patterns with all the number of fringes in the set $\mathbb{S}_n$. The statistical properties of the random noise in relative phase can be estimated from the distribution of phase values from repeated measurements. The relative phase value of each pixel can be obtained using all-in-focus (AIF) images of phase-shifted patterns, where the AIF images are acquired using the method described in Sec. 4.2. In this work, we use three phase-shifted patterns. The relative phase value of each pixel is obtained by[22]

$$\phi^c(x,y) = \arctan\left\{\frac{\sqrt{3}\cdot[I_1^C(x,y) - I_3^C(x,y)]}{2\cdot I_2^C(x,y) - I_1^C(x,y) - I_3^C(x,y)}\right\}, \quad (2)$$

where the pixel coordinates (x,y) represent coordinates in the camera coordinate frame C and I_1^C, I_2^C, I_3^C correspond to the intensity of the three phase-shifted captured patterns, respectively. In addition, to take into account the effect of shallow DOF of microscope optics, e.g., the noise introduced by unfocused images, the noise in phase values is determined at different positions along the z-axis (depth dimension) within the target measurement volume. The end result of this process is a full characterization of the noise in phase values, as a function of z-position and the number of fringes of the pattern projected.

The last task in the methodology is to identify the set of fringe patterns for sequential phase unwrapping. This set minimizes the random noise in the absolute phase that results from the sequential phase unwrapping. The absolute phase of a pixel is determined by[22]

$$\Phi_{n_f}^{C,k}(x,y) = 2\pi\,\mathrm{round}\left[\frac{n_f\cdot\Phi_{\mathrm{ref}}^{C,k-1}(x,y) - \phi_{n_f}^C(x,y)}{2\pi}\right] + \phi_{n_f}^C(x,y), \quad (3)$$

where $\Phi_{n_f}^{C,k}$ is the absolute phase at the current (k) phase unwrapping step resulting from the relative phase $\phi_{n_f}^C$ of a pattern with n_f fringes and the reference phase $\Phi_{\mathrm{ref}}^{C,k-1}(x,y)$ is the absolute phase from the previous unwrapping step $(k-1)$ or from the single-fringe pattern (when $k=1$). The effect of the random noise introduced during phase unwrapping is simulated for the set of fringes by (1) creating a set of ideal images of the fringe patterns; (2) determining ideal relative phase values from these images using Eq. (2); (3) adding random noise to these relative phase values based on the range of noise levels estimated on the previous task of the methodology; (4) determining the absolute phase using phase unwrapping, i.e., Eq. (3), for the set of multifringe patterns; and (5) determining the standard deviation of the resulting absolute phase when varying the random noise level. Hence, for each unwrapping step, the number of fringes in the multifringe pattern is determined by minimizing the noise level. Namely, the number of fringes that minimizes the norm of the gradient of the random noise of the absolute phase[16]

$$\arg\min_{nf} \iint \|\nabla\sigma_{\Phi_{n_f}^C}\|^2 \mathrm{d}\sigma_{\Phi_{\mathrm{ref}}^C}\,\mathrm{d}\sigma_{\phi_{n_f}^C}, \quad (4)$$

where σ denotes the standard deviation of the random noise in phase and $\|\nabla\sigma_{\Phi_{n_f}^C}\|^2$ corresponds to the L_2-norm of the gradient of $\sigma_{\Phi_{n_f}^C}$. The L_2-norm of the gradient is integrated over the range of noise levels estimated in the second step of the methodology. Sequential unwrapping terminates when there is <1% random noise improvement between the $k-1$ unwrapping step and the k unwrapping step

$$\left\|\frac{\sigma_{\Phi^C_{n_f,\mathrm{step}_k}} - \sigma_{\Phi^C_{n_f,\mathrm{step}_{k-1}}}}{\sigma_{\Phi^C_{n_f,\mathrm{step}_{k-1}}}}\right\| \le 0.01. \quad (5)$$

4 Calibration of SL System for Microscale Measurements

Once the SL systems have been implemented using an optimal hardware configuration and pattern sequence, we use an empirical calibration model to predict the world coordinates of the object surface. Our proposed calibration approach provides one global model valid for all pixels in the captured images; hence, it simultaneously considers data from multiple pixels to capture variable interactions (e.g., caused by radial distortion, optical aberrations, or varying focus settings). A single empirical calibration model can be used to characterize the relation between image coordinates, projector coordinates, and world coordinates due to the use of multifocus imaging and fusion, which creates a single all-in-focus image. The empirical approach allows for modeling of the relationship between coordinates independent of the internal parameters of the camera, which may vary using our multifocus imaging and fusion method.[1] This calibration model can reduce the variance of the estimated model parameters and model predictions.

The calibration procedure, shown in Fig. 3, consists of the following steps: (1) multifocus imaging of the calibration object within the desired measurement volume, (2) focus fusion of images obtained in step 1 to generate all-in-focus images of the fringe patterns, (3) image feature detection of features on the calibration object for determining world coordinates on the calibration object, (4) image feature remapping from camera to projector image coordinate frame using the absolute phase to correlate camera pixel, projector image, and 3-D spatial coordinates, and (5) model fitting to the acquired data set and selection of the best-fitting model. Once the system is calibrated, only steps 1 and 2 followed by the application of the fitted model would be required for measuring an object of interest.

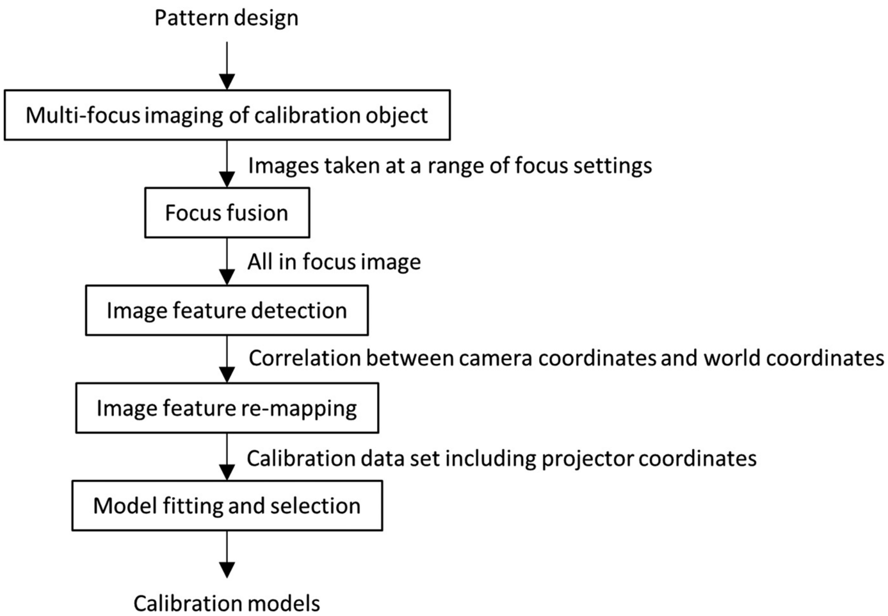

Fig. 3 Calibration procedure for SL system for microscale measurements.

4.1 *Multifocus Imaging of the Calibration Object*

In this step, the calibration object is imaged under multiple focus settings, at various positions within the measurement volume, and under different illumination conditions. The calibration object containing a grid of markers with known size and spacing is placed on a precision stage and gradually moved with fixed steps of equal distance along the z-axis, which is aligned with the depth dimension. Images are captured for the calibration object at each position, starting from the farthest position ($Z_W = 0$) to the closest z-position to the sensory system. Then, the object is returned to the $Z_W = 0$ position and moved with fixed steps of equal distance in the y-direction, and the process is repeated multiple times so that the calibration object markers form a dense grid within the measurement volume. This dense grid ensures that the calibration model (Sec. 4.5) has enough data to provide accurate predictions of the world coordinates of the object surface when obtaining surface profile measurements (Sec. 6).

At each position of the calibration object, the fringe patterns are projected and captured using different focus settings of the optics. This ensures that each region of the measured object has been captured, in focus and illuminated for each pattern. In addition, fully illuminated images (with no fringes) are captured at the same set of focus settings; these images are used during the focus fusion step, described next. The end result of this process is a set of $n_{\text{focus}} \times (n_{\text{patterns}} + 1)$ images, where n_{focus} is the number of focus settings and n_{patterns} is the number of fringe patterns, incremented by 1 to account for the fully illuminated images. When capturing images at a range of focus setting, motors are used to automate the change in focus settings.

4.2 *Focus Fusion*

After the images with different focus settings have been captured, a post-processing step is performed to fuse images from multiple focus settings into a single AIF image for each fringe pattern. First, the fully illuminated images of the object are fused with the selective all-in-focus (SAF) algorithm,[31] as shown in Fig. 4. The SAF algorithm starts by determining a focus measure for each pixel in each image and a selectivity measure that quantifies the deviation of this focus measure from its ideal Gaussian behavior. Then, each pixel of the AIF image is computed as a weighted average of the intensity values of that pixel in all the input images, using the selectivity measure as weights. These weights are then used to fuse the images of the light patterns captured at the same focus settings. We do this to reduce the potential errors that may be introduced if focus fusion is directly applied to the fringe pattern images due to the varying illumination of the fringe patterns themselves.

4.3 *Image Feature Detection*

The next step in the calibration approach is to automatically detect features in the images of the calibration object, namely its circular markers. The AIF fully illuminated image is used to determine the image camera coordinates (u_C, v_C) of each marker at each z-position using an automated feature detection algorithm. A Hough transform[31] is used in this work to identify the image coordinates of the calibration object markers, due to its robustness to the presence of noise in the images. The final result of the image feature detection step is a data set of n_{calib} points containing the world coordinates of the calibration object markers $(X_{W,k}, Y_{W,k}, Z_{W,k})$, known from the position of the motion stages, and the image coordinates of these points in the camera sensor $(u_{C,k}, v_{C,k})$, $k = 1, \ldots, n_{\text{calib}}$, determined from the captured images through the automated detection procedure.

4.4 *Image Feature Remapping*

In this step of the calibration procedure, the image coordinates of the calibration object markers are remapped to the projector panel. Previous steps of the calibration procedure have resulted in a data set $(X_{W,k}, Y_{W,k}, Z_{W,k}, u_{C,k}, v_{C,k})$, $k = 1, \ldots, n_{\text{calib}}$, containing the world and image coordinates of the calibration object markers. To complete this calibration data set, however, the image coordinates of the calibration object markers in the projector panel $(u_{P,k}, v_{P,k})$ must be determined. To this end, the coordinates of the markers are remapped to the projector viewpoint using the phase values of the pixels surrounding each calibration marker, as follows.

For the k'th calibration object marking, its coordinates in the projector panel, $(u_{P,k}, v_{P,k})$, are determined by first identifying the absolute phase values $(\Phi_{H,k}, \Phi_{V,k})$ that correspond to the image coordinates of the markers $(u_{C,k},\ v_{C,k})$ in the camera. Feature detection algorithms determine the image coordinates of the markers with subpixel accuracy (i.e., pixel coordinates are real numbers, not integers), while the absolute phase values are only available at integer pixel coordinates in the camera. Hence, a bilinear interpolation approach is used to determine $(\Phi_{H,k}, \Phi_{V,k})$ from the phase values captured by the camera at the pixels that surround the pixel $(u_{P,k}, v_{P,k})$, where the k'th calibration marking was detected. The bilinear interpolation can be expressed as

$$\Phi_{H,k}(u_{C,k}, v_{C,k}) = a_0 + a_1 u_{C,k} + a_2 v_{C,k} + a_3 u_{C,k} v_{C,k}, \quad (6)$$

$$\Phi_{V,k}(u_{C,k}, v_{C,k}) = b_0 + b_1 u_{C,k} + b_2 v_{C,k} + b_3 u_{C,k} v_{C,k}, \quad (7)$$

where a_i and b_i, $i = 0, \ldots 3$, are the interpolation coefficients. Once the absolute phase values $(\Phi_{H,k}, \Phi_{V,k})$ of the markers are known, the corresponding image coordinates in the projector panel $(u_{P,k}, v_{P,k})$ can be uniquely determined by linear interpolation.

4.5 *Model Fitting and Selection*

The final step in the calibration procedure consists of fitting a set of regression models to the calibration data and selecting the best fitting model among this set using statistical tools. In this work, a single empirical calibration model is used for all camera pixels to predict each 3-D world coordinate of each point on the object surface as a function of its camera and projector pixel coordinates, namely

$$X_W = f_X(u_c, v_c, u_p, v_p), \quad (8)$$

$$Y_W = f_Y(u_c, v_c, u_p, v_p), \quad (9)$$

$$Z_W = f_Z(u_c, v_c, u_p, v_p), \quad (10)$$

where u_c, v_c and u_p, v_p are the camera and projector image coordinates of the point on the object surface, respectively. X_W, Y_W, and Z_W are its coordinates in the world reference frame, and f_k, $k = X, Y, Z$ are regression functions with coefficients determined based on the calibration data set generated in the previous steps. LUT approaches used in the literature require creating one model similar to Eqs. (8)–(10) per each pixel in the image, each fitted only to data for that particular pixel. This results in a large number of models, each fitted to a very small set of data, yielding a larger prediction variance. Alternatively, the calibration approach that we propose in this work uses a single global model for each world coordinate that is fitted to data from all pixels and is thus able to capture the global trends and nonlinear interactions between input variables, which may arise due to image distortions, optical aberrations, or image shifts caused by changing focus settings. More importantly, using all pixel data to fit a single model for each world coordinate allows for a larger data set, which leads to more robust estimates for the calibration parameters and narrower confidence intervals for the model predictions, in contrast with LUT approaches.

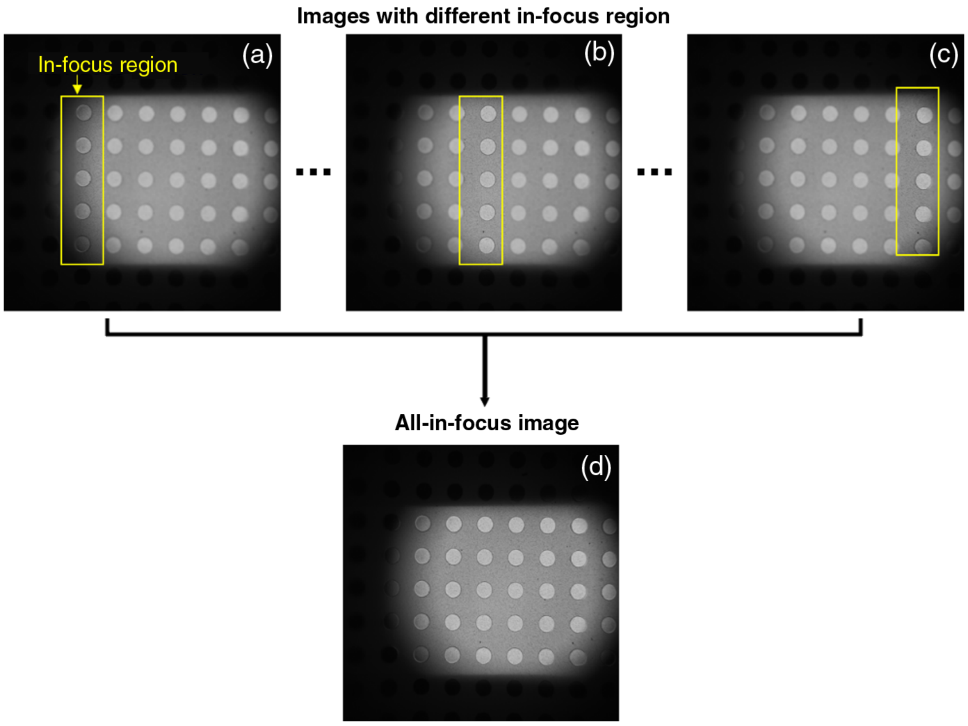

Fig. 4 Illustration of the focus fusion procedure. Images (a)–(c) are taken with different in-focus regions that are fused together to generate (d) a single all-in-focus image with all the regions in focus.

Based on previous work[8] that has used polynomial functions to establish phase-to-height relationships, in this work, polynomial regression functions up to third order are considered candidates for f_k. The choice of considering only polynomials of up to third order is based on the statistical principle of parsimony[32] and is further verified in this work through analysis of regression residuals and model selection metrics, discussed later in this section. The iteratively reweighted least squares (IRLS) method[33] is used to determine the coefficients for the candidate calibration models that are robust to outliers in the data, which may be caused by vibration, ambient illumination, object albedo, or other noise sources.

Once all the candidate calibration models are fitted to the calibration data, the model selection metrics below are used to select the best model for that particular data set.[32] In this context, the best model is defined as that which fits the data well without overfitting, thus exhibiting better generalization capabilities.[32] In particular, in this work, both the residual-mean-squared error and the leave-one-out cross-validation error are calculated, respectively, as

$$\mathrm{MS}_{\mathrm{res}}(p) = \frac{\mathrm{SSE}_{\mathrm{res}}(p)}{n - p}, \tag{11}$$

$$\mathrm{CV} = \sqrt{\frac{1}{n}\mathrm{PRESS}}, \tag{12}$$

where n is the number of observations; p is the number of model coefficients (a measure of "complexity" of the model); $\mathrm{SSE}_{\mathrm{res}}(p) = \sum_{i=1}^{n}(\hat{\mathbf{y}}_i - \mathbf{y}_i)^2$ is the sum of squared errors between the value of the i'th observation y_i and the value of the i'th observation predicted by the fitted model $\hat{y}_i$ for a regression model with p parameters; and $\mathrm{PRESS} = \sum_{i=1}^{n}(\hat{\mathbf{y}}_{-i} - \mathbf{y}_i)^2$ is the prediction sum of squares for leave-one-out cross validation, where $\hat{\mathbf{y}}_{-i}$ is the value of the i'th observation predicted by a model fitted to a data set from which this observation has been removed. Equations (11) and (12) above are model selection metrics commonly used in multivariable prediction; models with lower values of these metrics are preferred.

Following standard practices in model selection,[34] the calibration data set is split into two subsets. One data set, named the training data set and containing 80% of the observations, is used to determine the model coefficients and, using cross-validation approaches, to select the best model for the data. The second set, named the validation data set and containing the remaining 20% of the data, is used after the models are fitted and a model is selected to provide an unbiased assessment of its predictive abilities.

5 Development of an SL Sensory System for Microscale Measurements

This section presents the development of an SL system for microscale measurements following the proposed design methodology. The SL system developed consists of a DLP projector (Texas Instrument Inc. DLP Light Commander, 1024×748 pixel resolution) for projecting the fringe patterns onto the measured object, a CMOS camera (Adimec Quartz Q-4A180 camera, 2048×2048 pixel resolution) for capturing the deformed patterns, their corresponding LWD microscope lenses, and a microcontroller to synchronize the projection and capture of the fringe patterns, as shown in Fig. 5. The lenses used with the projector include a Nikon 45 mm f/2.8-D tilt-shift lens, a Fujinon CCTV 8-mm lens as reverse lens, a 20× Mitutoyo objective lens, and a 6.5× zoom microscope lens. The stackable microscope lenses of the camera include a 20× Mitutoyo infinity-corrected LWD microscope objective lens, a 6.5× motorized ultra-zoom microscope lens, and a 1.0× tube lens. The complete SL system was mounted on a passively damped optical table to minimize the effect of vibration on the experimental results.

5.1 *SL System Configuration*

The SL system for microscale measurements was developed and implemented following the steps of the design methodology presented and discussed in Sec. 3.1. The design methodology was applied to determine the optimal configuration of the hardware components shown in Fig. 5. The measurement volume for the SL system developed was defined to be $0.5 \times 0.5 \times 0.5\ \mathrm{mm}^3$.

5.2 *Pattern Sequence for Optimal System Configuration*

The optimal pattern sequence for the optimal SL system configuration was determined following the procedure discussed in Sec. 3.2.

5.2.1 *Set of fringes*

Step 1 of the proposed methodology was applied to determine the set of fringes $\mathbb{S}_n$ of the SL system. Since the horizontal resolution of the projector is 1024 pixels (direction used

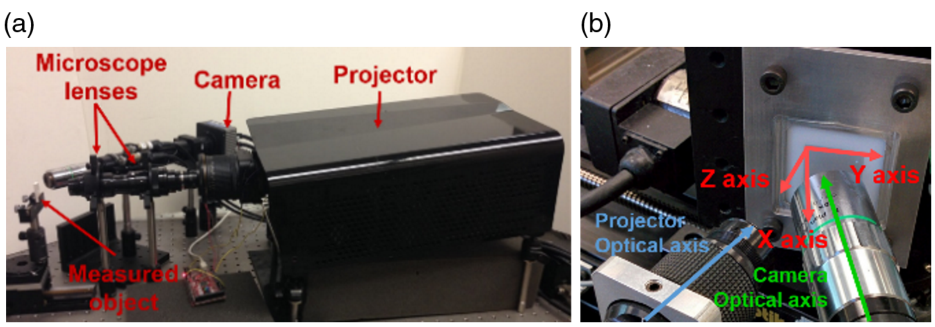

Fig. 5 (a) 3-D SL sensory system for microscale measurements and (b) world coordinate system indicated on the system setup.

for pattern encoding), the set of fringes is given by $\mathbb{S}_n = \{n_f\} = \{1, 2, 4, 8, 16, 32, 64, 128\}$, where n_f corresponds to the number of fringes that satisfies the two conditions of (1) $n_f \in \{1, \ldots, 1024/5\}$ and (2) $1024 \bmod n_f = 0$.

5.2.2 *Random noise in relative phase*

Step 2 of the procedure was used to determine the noise in phase values. Fringe patterns with all the number of fringes included in the set $\mathbb{S}_n$ were projected onto a vertical calibration plane placed within the measurement volume. The plane was moved to 11 different positions in 50-μm increments along the z-axis using a three-axis translational stage (Thor Labs PT3M). The random noise in phase was estimated by (1) taking repeated measurements of the plane for each z-position, (2) calculating the noise as the standard deviation of the phase values at each pixel with respect to the z-position, and (3) taking the average noise of all the pixels for each plane position. Figure 6 shows the average phase noise for each number of fringes at the different plane positions considered. The noise in relative phase increased when the plane was imaged at the positions $Z_W = \{0, 100, 450, 500\}$ μm, which corresponded to the positions that are outside the

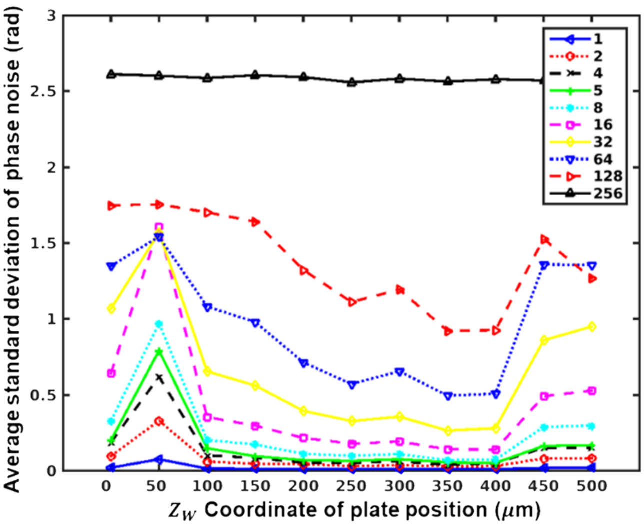

Fig. 6 Relative phase noise of fringe patterns projected onto a flat plane moved along the z-axis of the measurement volume for micro-scale measurements.

in-focus region. Hence, the measurement volume in which both the camera and the projector are in focus is defined to be within $Z_W =$ 100 and $Z_W = 400$ μm.

5.2.3 *Pattern sequence*

Step 3 of the procedure was implemented to determine the optimum set of multifringe patterns among the set of existing fringes determined in step 1. Based on Fig. 6, a value of 0.25 rad for the noise in relative phase was used, and $\eta = 1.5$ was considered; hence, the noise level was set to be within $0 < \sigma_{\phi^C_{n_f}} < 0.375$ rad, which provided an approximate upper bound for the phase noise for patterns with up to 64 fringes. The absolute phase $\tilde{\Phi}^C_{n_f}$ was simulated $N_{\text{reps}} = 20$ times for each random noise value defined by incrementing by 0.009 rad through the aforementioned range.

Equation (3) was used to identify the optimal set of patterns for the SL system. The number of unwrapping steps was determined to be four, resulting in patterns with $\{1, 2, 4, 8, 16\}$ fringes. Figures 7(a) and 7(b) show the results for the first and the last phase unwrapping steps where the random noise in the resulting absolute phase $\sigma_{\Phi^C_{n_f}}$ is presented in logarithmic scale as a function of the number of fringes n_f and the random noise level of the relative phase $\sigma_{\phi^C_{n_f}}$ and the reference phase $\sigma_{\Phi^C_{\text{ref}}}$. The larger number of fringes is represented with lighter shades in Fig. 7. For the first unwrapping step, Fig. 7(a), it can be seen that $n_{f,\text{step 1}} = 2$ fringes minimizes the random noise in the absolute phase for the entire range of $\sigma_{\phi^C_{n_f}}$ and $\sigma_{\Phi^C_{\text{ref}}}$. Similarly, after four unwrapping steps, Fig. 7(b), it can be seen that $n_{f,\text{step 4}} = 16$ fringes provides the minimum random noise in the resulting absolute phase.

5.3 *Calibration*

For system calibration, the procedure described in Sec. 4 was used. A planar calibration object, a 25×25 mm, 0.125-mm spacing, opal distortion target from Edmund Optics Inc.,[35] featuring a grid of circles with a radius of 62.5 μm and a spacing of 125 μm was used. The calibration object was mounted on top of the three-axis translational stage to move the calibration object through the measurement volume. The position repeatability of the stage is 1.5 μm.

The calibration plane was placed vertically on the stage, i.e., with the normal of the plane aligned with the z-axis. The

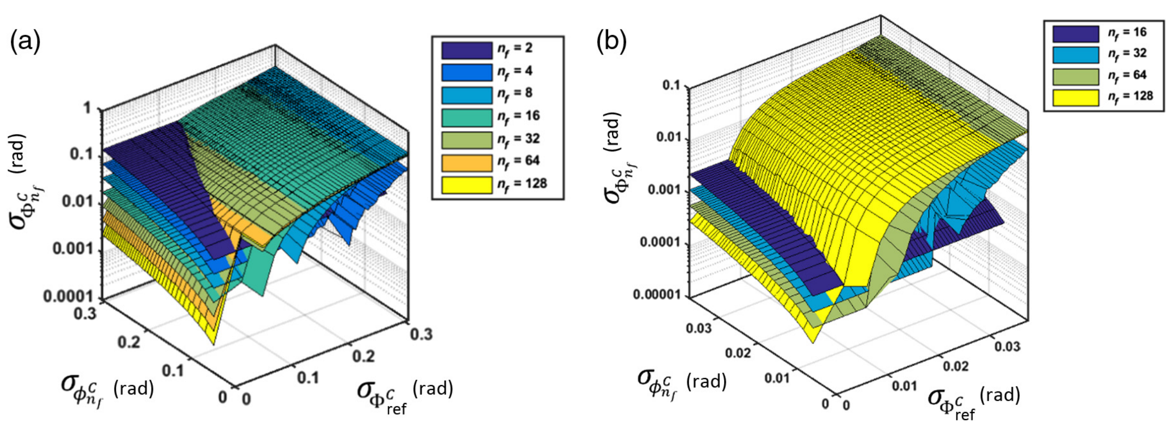

Fig. 7 Effect of random noise in relative and reference absolute phases on the absolute phase for varying random noise levels during (a) the first and (b) the fourth (last) unwrapping steps.

plane was gradually moved with a fixed step along the z-axis, in 50-μm steps, starting from the farthest ($Z_W = 0\ \mu$m) to the closest z-position ($Z_W = 500\ \mu$m) to the SL system. Then, the plane was returned to the position $Z_W = 0\ \mu$m and moved 20-μm steps in the y-direction a total of 6 times, each followed by another set of 50 μm movements in the z-direction. This procedure resulted in a total of 66 plane positions.

5.3.1 *Multifocus imaging of the calibration object*

For each position of the calibration object, the optimal pattern sequence, namely patterns with {1, 2, 4, 8, 16} fringes, was projected. In addition, for each position, a fully illuminated pattern was also projected for focus fusion. For each pattern, images were captured using a procedure for capturing images at multiple focus settings. This procedure consisted of (1) searching the peak focus of an image to determine the in-focus region, (2) varying the focus level to position the in-focus region at the left of the camera view, and (3) imaging the camera view with images at successive focus levels until the in-focus region was at the right of the camera view. This resulted in a collection of images with a small in-focus region that moved across the camera view.

5.3.2 *Focus fusion*

The images captured in the previous step were post-processed to combine the in-focus region from multiple images captured with different focus levels into a single AIF image for each fringe pattern at each calibration object location. The fully illuminated images were processed first to determine how to map the in-focus region from each image to the final AIF image. This mapping was then used for the focus fusion of the remainder pattern images.

5.3.3 *Image feature detection*

The circular Hough transform,[30] a circle detection algorithm based on the Hough transform, was used to determine the location of the centers of the circular markings in the calibration object. The world coordinates of the circle centers were defined based on the known position of the stage and the known distances between circle centers. This information was combined with the image coordinates (u_c, v_c) of the circle centers in the camera. A total of ∼1000 data points were used for calibration.

5.3.4 *Image feature remapping*

The last step in acquiring the calibration data was determining the image coordinates in the projector panel (u_P, v_P) for each of the circle centers, which required determining the pixel-to-pixel correspondences between the camera and the projector. Hence, the absolute phases of each pixel were obtained by sequential phase unwrapping of the AIF images of the optimal pattern set {1, 2, 4, 8, 16}. Finally, the absolute phase values of each pixel were used to calculate the image coordinates of each detected circle center in the projector. This completed the calibration data set, i.e., $(X_{W,k}, Y_{W,k}, Z_{W,k}, u_{C,k}, v_{C,k}, u_{P,k}, v_{P,k})$, for $k = 1, \ldots, n_{\text{calib}}$.

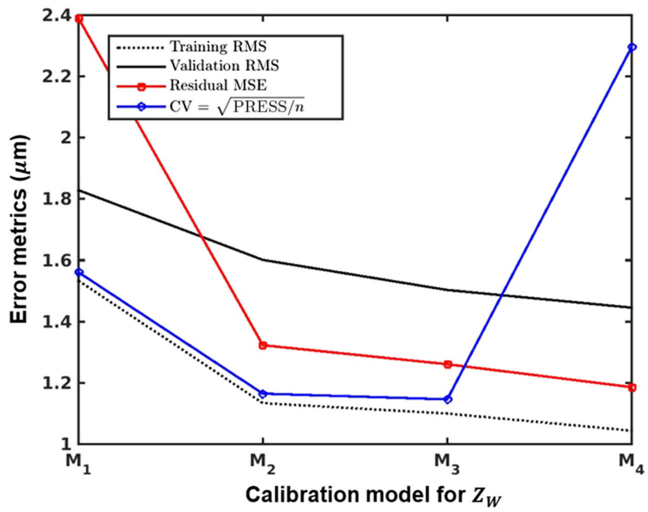

Fig. 8 Error metrics and model selection metrics estimating the z-coordinates using the calibration models: M1, linear; M2, linear with interactions; M3, quadratic; M4, cubic.

5.3.5 *Model fitting and selection*

The calibration data set obtained was used to fit candidate regression models to map the camera and projector image coordinates of points on the object surface to the corresponding world coordinates. The training data set was used to determine the coefficients of the model that best fit the data, while the validation set was utilized to assess the predictive performance of the models with a data set that was not used during model fitting.

As discussed in Sec. 4.5, polynomial models of first, second, and third degree were fitted to the training data set using IRLS. Then, model selection metrics were computed using the training data to select the single best predictive model for each world coordinate. Figure 8 shows the behavior of error metrics (training RMS, validation RMS) and model selection metrics (residual MSE, cross-validation error) for the model for predicting the Z_W coordinates. Models for the X_W and Y_W presented similar behavior for the error metrics as Z_W. As expected, the RMS error of the model for the training data set decreases as models with more explanatory variables (and more tunable coefficients) are considered. Note, however, that the cross-validation (CV) error increases for the M_4 (i.e., cubic) model, exhibiting its lowest value for the M_3 (i.e., quadratic) model in all three cases. This is evidence that the cubic model is overfitting the data and is thus unable to predict new observations accurately even though they reproduce the training data closely. Similar behavior of both training and cross-validation errors is expected for all higher order models.[32] Based on this evidence, the quadratic model was selected for the calibration data set for all three coordinates. Table 1 shows the resulting calibration model and its coefficients obtained from the calibration data.

6 Experiments

Once the calibration of the SL system for microscale measurements was completed, a series of tests was performed to assess the performance of our design methodology and calibration procedure. Both a planar object and complex objects were used for these tests, as discussed below. The

Table 1 Calibration model and coefficients for the SL system.

Coordinate	Calibration model
	$\beta_0 + \beta_1 u_c + \beta_2 u_c^2 + \beta_3 v_c + \beta_4 u_c v_c + \beta_5 v_c^2 + \beta_6 u_p + \beta_7 u_c u_p + \beta_8 v_c u_p + \beta_9 u_p^2$
X_W	$\overrightarrow{\beta_X} = =$ [−1.1832, 0.0141, −0.0267, 2.4420, −0.0073, 0.0002, −0.1285, 0.0662, −0.0054, −0.0159]
Y_W	$\vec{\beta_Y} =$ [−1.8035, 1.9230, −0.0655, 0.0133, 0.0008, 0.0002, 1.3125, 0.1914, 0.0132, −0.1170]
Z_W	$\vec{\beta_Z} =$ [−1.1020, −8.4957, 0.2071, −0.0223, −0.0105, −0.0052, 9.3165, −0.2730, 0.0847, 0.1714]

performance metrics used were (1) the measurement accuracy of the system and (2) surface profile measurements with depth variations and surface discontinuities.

6.1 *Planar Object*

A planar object, the calibration object described in Sec. 5.3 above, was placed vertically on the stage, i.e., with the normal of the object plane aligned with the z-axis of the SL system. The planar object was moved along the z-axis, imaged with multiple focus settings using both full illumination and the fringe patterns, to generate a set of AIF images following the same approach used for calibration. Different focus settings can be used for the calibration and measurement stages.

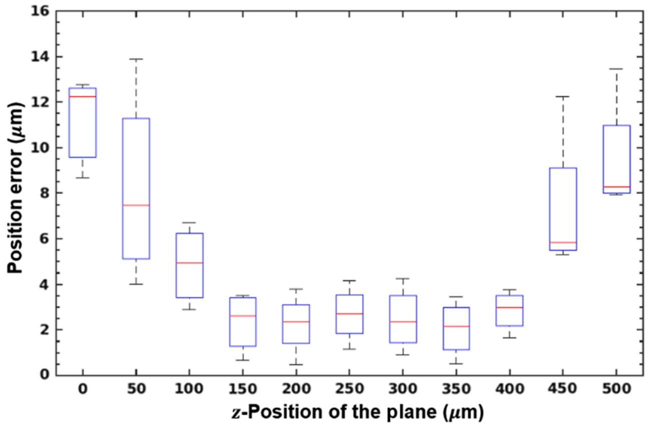

Fig. 9 Plane position error with respect to the stage position within the measurement volume.

It is only required that the images taken at these focus settings have complementary in-focus regions that cover the object. As long as this condition is satisfied, AIF images of the object can be obtained. The plane was moved 10 times in 50-μm steps from $Z_W = 0$ μm to $Z_W = 500$ μm and moved 3 times in 20-μm steps along the y-direction, for a total of 44 plane positions.

At each position, the planar object was measured using the absolute phase maps from the fringe pattern sequence. Then, using the calibration model, the world coordinates of each pixel were calculated, thus generating the point clouds. A mathematical model representing a plane was fitted to each point cloud using linear regression. The mean value of the Z_W coordinates of the point clouds was used to determine the z-position of the plane, which was compared with the actual position of the stage. Figure 9 shows the position errors, i.e., the difference between the z-position of the fitted plane and the (known) position of the stage. The errors are larger when the planar object is placed at $Z_W = \{0, 50, 450, 500\}$ μm, which coincide with the positions where the phase noise errors were larger. However, median position errors for the central region of the measurement volume, i.e., when the planar object was placed at $Z_W = \{150, \ldots, 400\}$ μm are under 3 μm.

6.2 *Complex Objects*

The SL system was then used to measure features with different surface complexities such as straight and curved edges on a 10-cent Canadian coin and both convex and concave regions on small teeth of a gear from the mechanism of a wrist watch, Fig. 10. Figure 11 shows the surface profiles obtained for the number "3" and the letter "N" of the coin.

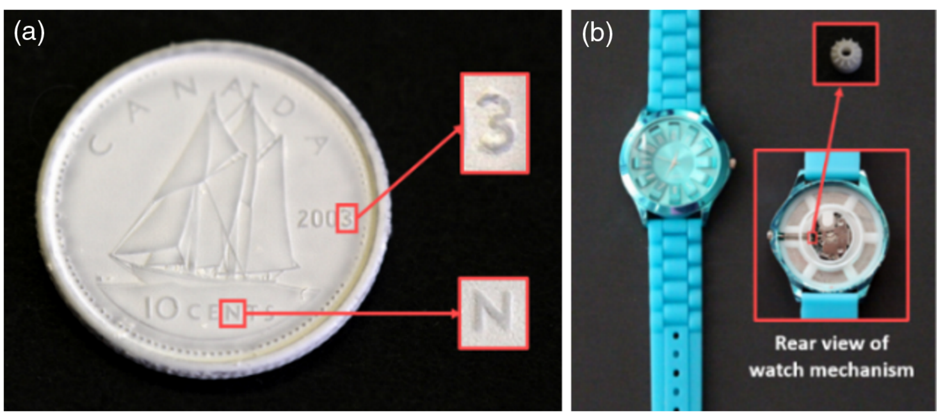

Fig. 10 Objects measured with the designed SL system: (a) microscale features "3" and "N" from a Canadian 10-cent coin (18 mm diameter) and (b) microscale gear from a wrist watch.

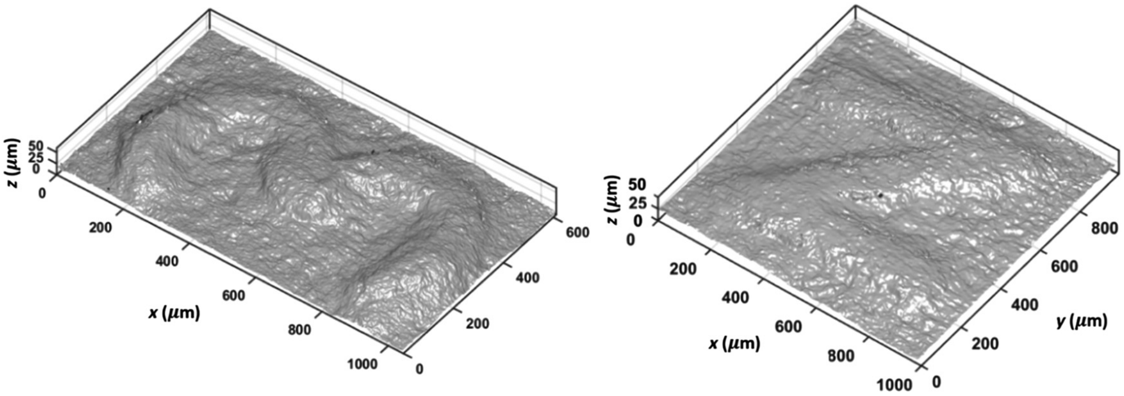

Fig. 11 Surface profile of the microscale features "3" and "N" on a Canadian dime measured with the designed SL system.

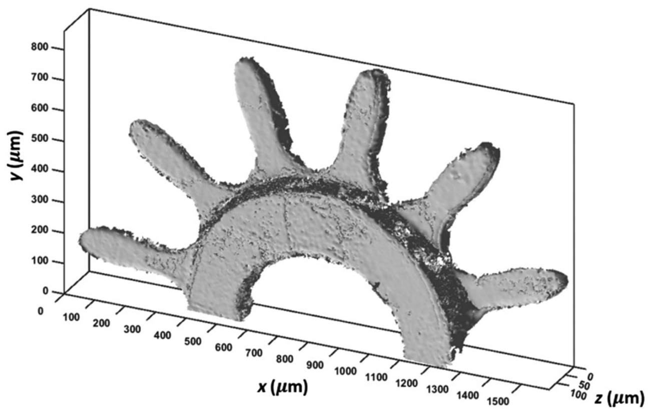

Fig. 12 Surface profile of the microscale gear of wrist watch measured with the designed SL system.

Figures 11(a) and 11(b) were rendered from a point cloud with >2 million points obtained by registration of 5 and 12 measurements, respectively. The surface profiles show the ability of the SL system to measure height variations on the coin.

Figure 12 shows the results of measuring teeth on the microscale gear. This surface profile was rendered from a point cloud with 4.5 million points, obtained by registration of 7 measurements. The surface profile of the microscale gear shows that the SL system is able to provide 3-D measurements of objects with varying curvatures.

7 Conclusions

In this paper, a comprehensive design methodology and calibration procedure were presented for the design and implementation of 3-D SL systems using image focus fusion for microscale measurements of objects. To the best of our knowledge, no previous work has developed and integrated a formal procedure to design and implement SL systems for microscale measurements. The proposed methodology considers the optical specifications to determine the triangulation configuration that maximizes the size of the measurement volume and the set of multifringe patterns that minimizes the random noise in the 3-D measurements introduced by the microscope magnification.

An empirical calibration approach using a global model was proposed and implemented. In contrast with previous work that fits one regression model for each pixel to predict surface height from phase data, the proposed empirical calibration model is globally valid throughout the measurement volume to accurately provide 3-D coordinates from phase data. This global model has the advantage of reduced measurement errors, due to the fact that more samples are used to estimate the model coefficients and interaction terms between the independent variables (i.e., the camera and projector pixel coordinates of a given surface point). In addition, the inclusion of such interactions allows the model to compensate for image distortions that may be caused by combining images from multiple focus settings to generate measurements.

An SL system for microscale measurements using image focus fusion was designed using the proposed methodology and calibration procedure. Its optimal configuration of the hardware components and its optimal pattern sequence were implemented. Experiments conducted with the system and varying objects demonstrated the effectiveness of the proposed approach for microscale measurements.

Disclosures

The authors have no relevant financial interests in the manuscript and no other potential conflicts of interest to disclose.

Acknowledgments

This research was funded in part by the Natural Sciences and Engineering Research Council of Canada through the Canadian Network for Research and Innovation in Machining Technology (NSERC CANRIMT) and the Canada Research Chairs (CRC) Program. The authors would like to thank E. Du and Y. Shiwakoti for their assistance in developing the 3-D sensory system.

References

1. J. Chen et al., "Microscopic fringe projection system and measuring method," *Proc. SPIE* **8759**, 87594U (2013).
2. M. Boissenin et al., "Computer vision methods for optical microscopes," *Image Vision Comput.* **25**(7), 1107–1116 (2007).
3. N. N. Moghadam, H. Farhadi, and M. Bengtsson, "An energy efficient communication technique for medical implants/micro robots," in *Proc. Int. Symp. on Medical Information and Communication Technology (ISMICT)*, pp. 1–5 (2016).
4. C. M. Caffrey, K. Twomey, and V. I. Ogurtsov, "Development of a wireless swallowable capsule with potentiostatic electrochemical sensor for gastrointestinal track investigation," *Sens. Actuators B* **218**, 8–15 (2015).

5. P. He et al., "Compression molding of glass freeform optics using diamond machined silicon mold," *Manuf. Lett.* **2**(2), 17–20 (2014).
6. K. Fregene and C. L. Bolden, "Dynamics and control of a biomimetic single-wing nano air vehicle," in *Proc. American Control Conf.*, pp. 51–56 (2010).
7. C. Quan et al., "Microscopic surface contouring by fringe projection method," *Opt. Laser Technol.* **34**(7), 547–552 (2002).
8. Y. Liu and X. Su, "High precision phase measuring profilometry based on stereo microscope," *Optik* **125**(19), 5861–5863 (2014).
9. J. Kettel, C. Müller, and H. Reinecke, "Three-dimensional reconstruction of specular reflecting technical surfaces using structured light microscopy," *Proc. SPIE* **9276**, 927609 (2014).
10. S. Van der Jeught, J. A. M. Soons, and J. J. J. Dirckx, "Real-time microscopic phase-shifting profilometry," *Appl. Opt.* **54**(15), 4953–4959 (2015).
11. C. Quan et al., "Shape measurement by use of liquid-crystal display fringe projection with two-step phase shifting," *Appl. Opt.* **42**(13), 2329–2335 (2003).
12. C. Quan et al., "Shape measurement of small objects using LCD fringe projection with phase shifting," *Opt. Commun.* **189**(1–3), 21–29 (2001).
13. P. Heidingsfelder, J. Gao, and P. Ott, "Theoretical analysis of photon noise limiting axial depth resolution for three-dimensional microscopy by incoherent structured illumination," *Opt. Eng.* **51**(10), 103203 (2012).
14. Y. Yin et al., "Fringe projection 3D microscopy with the general imaging model," *Opt. Express* **23**(5), 6846–6857 (2015).
15. L. Soto, H. Chuaqui, and R. Saavedra, "Interferometry of phase microinhomogeneities within macroscopic objects," *Meas. Sci. Technol.* **8**(8), 875–879 (1997).
16. S. H. Wang and C. J. Tay, "Application of an optical interferometer for measuring the surface contour of micro-components," *Meas. Sci. Technol.* **17**(4), 617–625 (2006).
17. V. Kebbel, H.-J. Hartmann, and W. P. O. Jueptner, "Application of digital holographic microscopy for inspection of micro-optical components," *Proc. SPIE* **4398**, 189–198 (2001).
18. X. Song, B. Zhao, and H. Wang, "Imaging and measurement of microscopic object by digital holographic microscopy," in *Proc. IEEE Int. Conf. Information Engineering and Computer Science*, pp. 1–4 (2009).
19. F. Blais, "Review of 20 years of range sensor development," *J. Electron. Imaging* **13**(1), 231–240 (2004).
20. J. Guehring, "Dense 3D surface acquisition by structured light using off-the-shelf components," *Proc. SPIE* **4309**, 220–231 (2000).
21. V. E. Marin, W. H. W. Chang, and G. Nejat, "Generic design methodology for the development of three-dimensional structured-light sensory systems for measuring complex objects," *Opt. Eng.* **53**(11), 112210 (2014).
22. V. E. Marin and G. Nejat, "Determining optimal pattern sequences for three-dimensional structured light sensory systems," *Appl. Opt.* **55**(12), 3203–3213 (2016).
23. S. Zhang and P. S. Huang, "Novel method for structured light system calibration," *Opt. Eng.* **45**(8), 083601 (2006).
24. Z. Zhang, "A flexible new technique for camera calibration," *IEEE Trans. Pattern Anal. Mach. Intell.* **22**(11), 1330–1334 (2000).
25. B. Li and S. Zhang, "Flexible calibration method for microscopic structured light system using telecentric lens," *Opt. Express* **23**(20), 25795–25803 (2015).
26. R. Orghidan et al., "Structured light self-calibration with vanishing points," *Mach. Vision Appl.* **25**(2), 489–500 (2014).
27. Y. An et al., "Method for large-range structured light system calibration," *Appl. Opt.* **55**(33), 9563–9572 (2016).
28. B. Li, N. Karpinsky, and S. Zhang, "Novel calibration method for structured-light system with an out-of-focus projector," *Appl. Opt.* **53**(16), 3415–3426 (2014).
29. P. Wang et al., "Calibration method for a large-scale structured light measurement system," *Appl. Opt.* **56**(14), 3995–4002 (2017)
30. G. Frankowski, M. Chen, and T. Huth, "Real-time 3D shape measurement with digital stripe projection by Texas instruments micro mirror devices DMD," *Proc. SPIE* **3958**, 90–105 (2000).
31. S. Pertuz et al., "Generation of all-in-focus images by noise-robust selective fusion of limited depth-of-field images," *IEEE Trans. Image Process.* **22**(3), 1242–1251 (2013).
32. L. Wassermann, *All of Statistics. A Concise Course in Statistical Inference*, Springer, New York (2004).
33. D. C. Montgomery, E. A. Peck, and G. G. Vining, *Introduction to Linear Regression Analysis*, John Wiley and Sons, Inc., New York (2001).
34. E. Alpaydin, *Introduction to Machine Learning*, MIT Press, Cambridge (2014).
35. Edmund Optics Inc., "25×25 mm, 0.125 mm spacing, opal distortion target," https://www.edmundoptics.com/test-targets/distortion-test-targets/25-x-25mm-0.125mm-spacing-opal-distortion-target/ (08 October 2017).

Veronica E. Marin received her undergraduate degrees in electronics engineering in 2002 and mechanical engineering in 2003, her MSc degrees in mechanical engineering in 2009 and applied computing in 2010, and her PhD in mechanical and industrial engineering from the University of Toronto, Canada, in 2016. She is a systems analyst at Thales Transportation Solutions. Her research interests are in robotics, mechatronics system design, computer vision, and autonomous transportation.

Zendai Kashino received his undergraduate degree in engineering physics from the University of British Columbia in 2015. He is currently pursuing his PhD in mechanical and industrial engineering at the University of Toronto, under the supervision of Prof. Beno Benhabib and Prof. Goldie Nejat, with a focus on autonomous wilderness search and rescue and optical metrology.

Wei Hao Wayne Chang received his BASc degree in mechanical engineering in 2011 from the University of Toronto and his MASc degree in mechanical and industrial engineering in 2014 after working in the Autonomous Systems and Biomechatronics Laboratory of University of Toronto. His research interests include the design and implementation of intelligent perception for autonomous high-speed meso/micromilling applications.

Pieter Luitjens received his MEng degree in mechanical and industrial engineering in 2015 after working in the Autonomous Systems and Biomechatronics Laboratory, University of Toronto.

Goldie Nejat is an associate professor in the Department of Mechanical and Industrial Engineering at the University of Toronto, where she is also the director of the Autonomous Systems and Biomechatronics Laboratory. Her current research interests include the development of three-dimensional sensory systems, and control and intelligence techniques for autonomous systems and assistive/service robots for manufacturing, search and rescue, exploration, and healthcare applications.